

# $\eta$ Carinae: a very large hadron collider

R. Walter<sup>1,2</sup>, C. Farnier<sup>1,2</sup>, J.-C. Leyder<sup>1,3,\*</sup>

<sup>1</sup> INTEGRAL Science Data Centre, Université de Genève, Chemin d'Ecogia 16, CH-1290 Versoix, Switzerland

<sup>2</sup> Observatoire de Genève, Université de Genève, Chemin des Maillettes 51, CH-1290 Sauverny, Switzerland

<sup>3</sup> Institut d'Astrophysique et de Géophysique, Université de Liège, Allée du 6-Août 17, Bâtiment B5c, B-4000 Liège, Belgium

Received < date >; Accepted < date >

## ABSTRACT

**Context.**  $\eta$  Carinae is the colliding wind binary with the largest mass loss rate in our Galaxy and the only one in which hard X-ray emission has been detected.

**Aims.**  $\eta$  Carinae is therefore a primary candidate to search for particle acceleration by probing its gamma-ray emission.

**Methods.** We used the first 21 months of *Fermi*/LAT data to extract gamma-ray (0.2 – 100 GeV) images, spectra and light-curves, then combined them with multi-wavelength observations to model the non-thermal spectral energy distribution.

**Results.** A bright gamma-ray source is detected at the position of  $\eta$  Carinae. Its flux at a few 100 MeV corresponds very well to the extrapolation of the hard X-ray spectrum towards higher energies. The spectral energy distribution features two distinct components. The first one extends over the keV to GeV energy range, and features an exponential cutoff at  $\sim 1$  GeV. It can be understood as inverse Compton scattering of ultraviolet photons by electrons accelerated up to  $\gamma \sim 10^4$  in the colliding wind region. The expected synchrotron emission is compatible with the existing upper limit on the non-thermal radio emission. The second component is a hard gamma-ray tail detected above 20 GeV. It could be explained by  $\pi^0$ -decay of accelerated hadrons interacting with the dense stellar wind. The ratio between the fluxes of the  $\pi^0$  and inverse Compton components is roughly as predicted by simulations of colliding wind binaries. This hard gamma-ray tail can only be understood if emitted close to the wind collision region. The energy transferred to the accelerated particles ( $\sim 5\%$  of the collision mechanical energy) is comparable to that of the thermal X-ray emission.

**Conclusions.** We have measured the electron spectrum responsible for the keV to GeV emission and detected an evidence of hadronic acceleration in  $\eta$  Carinae. These observations are thus in good agreement with the colliding wind scenario suggested for  $\eta$  Carinae.

**Key words.** Gamma rays: stars – X-rays: binaries – X-rays: individuals:  $\eta$  Carinae – X-rays: individuals: FGL J1045.0-5942 – Acceleration of Particles

## 1. Introduction

About 30 early-type stellar systems feature synchrotron radiation in the radio domain, a signature of electron acceleration (De Becker 2007). Diffusive shock acceleration in stellar wind collisions (Benaglia & Romero 2003), either in colliding wind binaries or OB associations, is the most likely acceleration process and a candidate for cosmic ray acceleration (Axford 1981; Casse & Paul 1982). Gamma-rays, emitted by hadrons accelerated in stellar wind collisions, have however not yet been identified.

The gamma-ray emission expected from a colliding wind binary increases with the stellar wind mechanical luminosity, the fraction of the wind enduring collision, the photon energy density for inverse Compton emission and the matter density for proton-proton interaction and subsequently  $\pi^0$ -decay. Located at a distance of 2.3 kpc (Smith 2006),  $\eta$  Carinae is one of the most massive (80–120  $M_{\odot}$ ; Davidson & Humphreys 1997; Hillier et al. 2001) and brightest stellar system in the Galaxy and features the strongest mass loss rate known. As, in addition, its colliding wind region is relatively wide,  $\eta$  Carinae is a primary candidate for gamma-ray detection.

The “Great Eruption” of 1843 saw  $\eta$  Carinae become the second brightest object in the sky; it was followed by another noteworthy flare in 1890 (see e.g. Davidson et al. 1999; Fernández-Lajús et al. 2010). The *Homunculus* is the name given to the extended bipolar nebula observed around  $\eta$  Carinae: it was crafted

by the colossal amount of matter (10–20  $M_{\odot}$ ; Smith et al. 2003) that was ejected during the Great Eruption. The second burst led to the ejection of  $\approx 1 M_{\odot}$ , creating the so-called *little homunculus*.  $\eta$  Carinae keeps emitting matter thanks to its powerful stellar winds: the mass-loss rate is believed to be  $10^{-4}$ – $10^{-3} M_{\odot} \text{ yr}^{-1}$  (Andriessse et al. 1978; Hillier et al. 2001; Pittard & Corcoran 2002; van Boekel et al. 2003).

Even if not all questions are settled, strong evidences suggest that  $\eta$  Carinae is a binary system. For instance, radio (Duncan et al. 1995), millimeter (mm; Abraham et al. 2005), optical (Damineli 1996; Damineli et al. 2000), near-infrared (near-IR; Whitelock et al. 1994, 2004; Damineli 1996), and X-ray (Corcoran 2005) observations, obtained over the last decades, have unveiled the existence of a period of  $\sim 2022.7 \pm 1.3$  days (Damineli et al. 2008).

The first component in the binary system is very likely a luminous blue variable (LBV; Davidson & Humphreys 1997). The second component is probably a late-type nitrogen-rich O or Wolf-Rayet (WR) star (Iping et al. 2005; Verner et al. 2005). The semi-major axis of the orbit is 16.64 AU (Hillier et al. 2001), and the eccentricity is very high ( $e \sim 0.9$ ; Nielsen et al. 2007). Thus, the periastron distance  $r_{\text{periastron}}$  is around 1.66 AU, while the primary star’s radius  $R_{\star,1}$ , although poorly constrained, is estimated between 0.7–1 AU (resp. Corcoran & Hamaguchi 2007; Damineli 1996).

The X-ray emission of  $\eta$  Carinae can be discriminated into two components, precisely known thanks to *Chandra* observations (Seward et al. 2001). The softer part ( $kT_{\text{SX}} \sim 0.5$  keV) pre-

Send offprint requests to: Roland.Walter@unige.ch

\* FNRS Research Fellow

arXiv:1008.2533v1 [astro-ph.HE] 15 Aug 2010

vails in the spectrum up to 1.5 keV. It is spatially extended, and is likely linked to the stellar winds colliding with the interstellar matter. The harder part ( $kT_{\text{HX}} \sim 4.7$  keV) dominates over the 2–10 keV domain. It is punctual, centered on the binary system, and believed to be due to the hydrodynamical shock created by the stellar winds of both components colliding with each other.

The X-ray spectrum of  $\eta$  Carinae supports the colliding-wind binary scenario (Usov 1992; Stevens et al. 1992; Corcoran 2005; Pittard 2007; Parkin et al. 2009). The basic idea is that the LBV emits a rather slow and dense stellar wind ( $v_{\infty,1} \approx 500$  km/s,  $\dot{M}_1 \approx 2.5 \times 10^{-4} M_{\odot}/\text{yr}$ ; Pittard & Corcoran 2002), which collides into the faster, shallower wind originating from the secondary component ( $v_{\infty,2} \approx 3000$  km/s,  $\dot{M}_2 \approx 1.0 \times 10^{-5} M_{\odot}/\text{yr}$ ; Pittard & Corcoran 2002). In this framework, the wind collision region represents the location of the hydrodynamical shock, and thus of the X-ray emitting region.

A hard X-ray tail had first been observed towards  $\eta$  Carinae by *BeppoSAX* (Viotti et al. 2004), and has subsequently been unambiguously confirmed by both *INTEGRAL* (Leyder et al. 2008, 2010) and *Suzaku* (Sekiguchi et al. 2009) observations. This gives a strong evidence that the wind collision leads to non-thermal electron acceleration, and suggests the possibility of a gamma-ray detection.

The Carina region has been observed with several gamma-ray experiments. *Agile* detected the source 1AGL J1043-5931 ( $\alpha=161.2$ ,  $\delta=-59.7$ , with an error of  $0.4^\circ$ ) that could be related to  $\eta$  Carinae (Tavani et al. 2009). A 2-day  $\gamma$ -ray flare has also been observed in October 2008, although its origin is unclear. *Fermi/LAT* detections were reported in the *Fermi* bright source list (BSL, Abdo et al. 2009) and in the first year catalog (1FGL, Abdo et al. 2010). In the BSL, the source 0FGL J1045.6-5937 lies at  $\approx 5.4$  arcmin of  $\eta$  Carinae and is therefore not associated with it. In the 1FGL, the source 1FGL J1045.2-5942 lies at 1.7 arcmin from  $\eta$  Carinae which is again too far for a formal identification. A possible association with the open cluster Trumpler 16, which may hold some energetic young pulsars, was suggested (Abdo et al. 2010). In the TeV domain, no detection has been reported in the vicinity of  $\eta$  Carinae.

In the following sections, we describe our detailed analysis of the *Fermi/LAT* data, and discuss the resulting multi-wavelength spectrum of  $\eta$  Carinae in terms of electronic and hadronic accelerations.

## 2. *Fermi/LAT* observations

The large area telescope (LAT) aboard the *Fermi* spacecraft is an electron-positron pair conversion telescope sensitive to photon energies from 20 MeV to  $> 300$  GeV (Atwood et al. 2009). The LAT is made of 16 towers, each including a particle tracker and a calorimeter (allowing for the reconstruction of the direction and energy of the incident gamma-ray photons), and of an anti-coincidence shield rejecting the charged particle background.

The data are provided by the Fermi Science Support Center<sup>1</sup>, which also delivers dedicated analysis software, called the *Fermi ScienceTools*<sup>2</sup>. The software modules allow to select events from an incoming region of the sky, to compute the corresponding live-time exposure map and the likelihood of an input sky model, and to derive significance maps, source spectra and light-curves.

<sup>1</sup> <http://fermi.gfsc.nasa.gov/>

<sup>2</sup> <http://fermi.gfsc.nasa.gov/ssc/data/analysis/software>

### 2.1. Data analysis

We have used *Fermi/LAT* data accumulated in the Carina region during 21 months, from August 4, 2008 to April 3, 2010. The reconstructed gamma-ray photons were selected in a circular region centered on  $\eta$  Carinae with a radius of  $10^\circ$ , belonging to the *diffuse class*<sup>3</sup>, and with energies between 200 MeV and 100 GeV. This upper limit is justified by the fact that at higher energies, systematics of the instrument and the role of cosmic-ray events are not yet fully understood. The low energy threshold was chosen for several reasons. Firstly,  $\eta$  Carinae is located in the Galactic plane, where the galactic diffuse emission (whose spectrum can be described by a powerlaw with a photon index of 2.2) is very strong. Selecting a threshold of 200 MeV decreases the number of background events by a factor of 4. Secondly, the galactic diffuse emission, whose knowledge is crucial to estimate the sky model parameters at low energies, is affected by large systematic uncertainties, influencing the likelihood analysis. Thirdly, the size of the LAT point spread function decreases rapidly with increasing energy (from 100 MeV to 200 MeV, the 68% event containment radius decreases from  $5^\circ$  to  $3^\circ$ ). As the analysed region encompasses a large number of sources (25 sources are listed in the 1FGL within  $10^\circ$  of  $\eta$  Carinae, out of which 10 are within  $3.5^\circ$ ), the ability to distinguish photons from different sources is important.

### 2.2. Localisation

The source 1FGL J1045.2-5942 ( $\alpha=161.3053$ ,  $\delta=-59.7057$ ) was not formally associated with  $\eta$  Carinae since the latter lies slightly outside of the 95% confidence region. As we are using almost twice more data than was available when the 1FGL was generated, a more accurate source localisation can be obtained. After an initial fit of the parameters of the sources close to the location of  $\eta$  Carinae, as well as of the normalisations of the diffuse galactic and isotropic emissions, we determined the position of the nearest source to  $\eta$  Carinae with the tool *gtfindsrc* and found  $\alpha=161.265$  and  $\delta=-59.7015$ , with a 95% confidence radius of 1.18 arcmin.  $\eta$  Carinae is thus perfectly compatible with our improved position, as illustrated in Fig. 1.

Since the width of the point spread function for photons converted in the front part of the LAT is smaller than for those converted in the back, we also derived the position using the front events only, but the uncertainty did not decrease significantly. We also derived the source location for low ( $< 8$  GeV) and high ( $> 10$  GeV) energy events and obtained error circles also compatible with the position of  $\eta$  Carinae (see Fig. 1).

The presence of the source is indubitable, with a test statistic (TS, Wilks 1938)  $> 2800$  ( $\approx 53 \sigma$ ) for the 200 MeV to 100 GeV energy range. The low and high-energy components have respectively TS of 2281 ( $\approx 47 \sigma$ ) and 73 ( $\approx 8.5 \sigma$ ). In the rest of the paper, we will name the *Fermi/LAT* source FGL J1045.0-5942, owing to its improved position.

### 2.3. Spectral analysis

The spectral analysis of FGL J1045.0-5942 was performed using the maximum likelihood method. The region modeling includes two diffuse emissions (Galactic plane and isotropic) and 35 point-like sources listed in the 1FGL catalogue. While most of these sources have been modeled as pure power-laws, four

<sup>3</sup> [http://www-glast.slac.stanford.edu/software/IS/glast\\_lat\\_performance.htm](http://www-glast.slac.stanford.edu/software/IS/glast_lat_performance.htm)

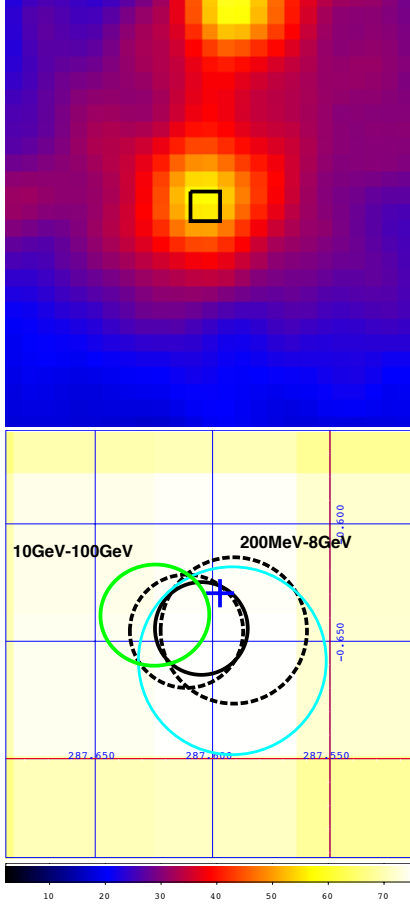


**Fig. 1.** *Top:* *Fermi/LAT* smoothed count map between 200 MeV and 100 GeV in galactic coordinates. The bright source in the centre of the field is FGL J1045.0-5942. The source located  $\sim 1.3^\circ$  to the North is the pulsar PSR J1048-5832. *Bottom:* *Fermi/LAT* significance map corresponding to a zoom on the black box shown in the upper image. The blue cross indicates the optical location of  $\eta$  Carinae. The green circle is the 95% confidence region reported for 1FGL J1045.2-5942 (based on 11 months of data). The plain black circle shows the 95% confidence region found in our analysis of the 21 month dataset. The dashed circles show the 200 MeV to 8 GeV and 10 GeV to 100 GeV confidence regions. The cyan circle corresponds to the confidence region of the hard X-ray detection obtained with *INTEGRAL* (Leyder et al. 2010).

among them are known to be pulsars and have thus been modeled as power-laws with exponential cutoff (Abdo et al. 2010). This is particularly important for the pulsar PSR J1048-5832, located  $\sim 1.3^\circ$  away from FGL J1045.0-5942.

As the detection of FGL J1045.0-5942 is very significant, a spectrum could be extracted in 9 spectral bins. In each bin, the TS is larger than 25 ( $5\sigma$ ). The resulting photon spectrum and spectral energy distribution are presented in Fig. 2. Both binned (Cash 1979) and un-binned (Mattox et al. 1996) likelihoods have been used and their results are in full agreement. A curvature at low energy and a modification of the spectral slope at high-energy are clearly detected.

The overall spectrum of FGL J1045.0-5942 differs from the standard power-law used to build the 1FGL catalogue, and has been modeled as a combination of two components: a power-law of photon index  $\Gamma$  with an exponential cutoff plus another

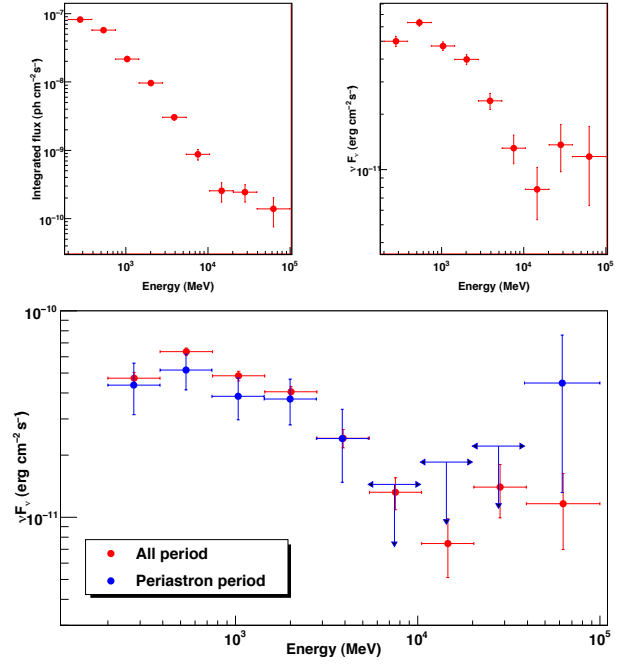


**Fig. 2.** *Top:* Photon spectrum (*left*) and spectral energy distribution (*right*) of FGL J1045.0-5942 with 21 months of *Fermi/LAT* data. *Bottom:* Spectral energy distribution for the complete 21 month period (red) and for the periastron period (blue). Uncertainties are 95% confidence levels.

power-law at the highest energies. Since only a limited number of spectral shapes are available in the *Fermi ScienceTools*, the dataset has been split into two energy ranges (0.2–8 GeV and 10–100 GeV) to determine the two spectral components independently. We maximized the sum of the likelihood in both spectral bands together so that the parameters of all sources are constrained by the complete dataset. The resulting parameters are  $\Gamma = 1.69 \pm 0.12$ ,  $E_{\text{cut}} = 1.8 \pm 0.5$  GeV,  $F_{0.2-100 \text{ GeV}} = 1.52 \times 10^{-7}$  ph cm $^{-2}$  s $^{-1}$  for the exponentially cutoff power-law and  $\Gamma = 1.85 \pm 0.25$ ,  $F_{0.2-100 \text{ GeV}} = 0.41 \times 10^{-7}$  ph cm $^{-2}$  s $^{-1}$  for the high-energy component.

#### 2.4. Timing analysis

We constructed the light-curve of FGL J1045.0-5942 using the maximum likelihood technique with time bins of one month (see Fig. 3). The light-curve is consistent with a steady flux. The time-averaged flux of the source in the 0.2–100 GeV energy range is  $F_{0.2-100 \text{ GeV}} = (1.93 \pm 0.05) \times 10^{-7}$  ph cm $^{-2}$  s $^{-1}$ .

The flux was also determined for the period when  $\eta$  Carinae was at the X-ray minimum, as measured by *RXTE*, (i.e. from MJD = 54843 to MJD = 54883). The flux level obtained for this period is reported in red in Fig. 3. It is compatible with the average flux at the 95% confidence level. The spectrum detected during the periastron period is also compatible with the average spectrum obtained over the 21 months period (bottom of Fig. 2). In particular the cutoff energy did not change significantly, nor the high-energy component, clearly detected above 40 GeV.

The gamma-ray emission does not vary by more than 50%, much less than observed in the X-ray band at periastron, where a variability factor larger than 10 is observed.

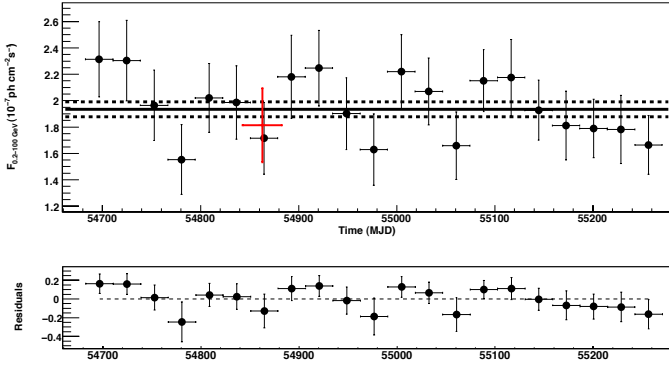


**Fig. 3.** *Top:* Monthly light-curve of FGL J1045.0-5942 derived from the 21 month *Fermi/LAT* dataset. The red point corresponds to the flux level observed during the X-ray minimum. The black line represent the best fit result (with its error) obtained assuming a steady flux for the source. Uncertainties are 95% confidence levels. *Bottom:* Residuals obtained from the steady flux fit.

Fig. 4 shows the high-energy ( $> 20$  GeV) events superimposed on the *RXTE* X-ray light-curve<sup>4</sup>. Despite the fact that this high-energy component is very significant ( $TS > 110$ ,  $\sigma > 10$ ), there is also no apparent correlation between the high-energy component and the orbital phase of  $\eta$  Carinae.

We also searched for gamma-ray flares using a flux aperture photometry method, but no significant deviation has been found. In particular, the two-day period during which *Agile* reported a flare from the Carina region has been investigated, but no sign of activity could be detected. During these two days, the average flux detected by *Fermi/LAT* is  $F = (1.9 \pm 0.6) \times 10^{-7} \text{ ph cm}^{-2} \text{ s}^{-1}$ , well below the flux detected by *Agile* which is  $(27.0 \pm 6.5) \times 10^{-7} \text{ ph cm}^{-2} \text{ s}^{-1}$  (Tavani et al. 2009). As *Fermi* and *Agile* have different orbits and as we used an energy threshold of 200 MeV, our analysis cannot exclude a very short and low energy flare.

### 3. Discussion

#### 3.1. Association with $\eta$ Carinae

Since the spectral energy distribution observed by *Fermi/LAT* is made of two components (Fig. 2), a spatial coincidence of two distinct gamma-ray sources (for instance a pulsar and a blazar) cannot be excluded a priori. However this coincidence should match with the centroids of the low- and high-energy components, which are separated by less than  $1.2'$  (Fig. 1) and compatible within the uncertainties. This is rather unlikely as this would require two bright gamma-ray sources very close to  $\eta$  Carinae.

Given the number of pulsars detected within  $2^\circ$  of the Galactic plane (26 or  $28^5$ ), the probability to find one of them in the 95% confidence region of  $\eta$  Carinae is  $2.5 \times 10^{-5}$ . Moreover, we conducted a blind search frequency analysis and did not find any evidence for a pulsation in FGL J1045.0-5942.

Given the 685 sources associated with blazars in the 1FGL over the entire sky, the probability to find a blazar at the location of  $\eta$  Carinae is  $2.3 \times 10^{-5}$ . In addition, if the high-energy emission was related to a blazar, flaring episodes would be expected, but none is observed (see Fig. 4).

<sup>4</sup> [ftp://legacy.gsfc.nasa.gov/xte/data/archive/ASMPProducts/definitive\\_1dwell/lightcurves/](ftp://legacy.gsfc.nasa.gov/xte/data/archive/ASMPProducts/definitive_1dwell/lightcurves/)

<sup>5</sup> The 1FGL quotes two potential  $\gamma$ -ray millisecond pulsars within  $2^\circ$  of the Galactic plane.

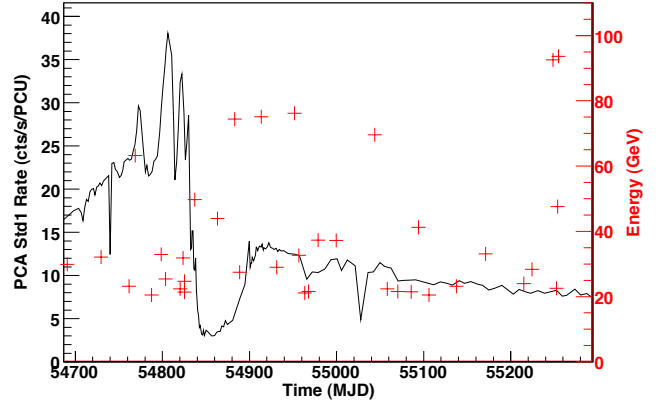


**Fig. 4.** The black line shows the *RXTE* X-ray light-curve of  $\eta$  Carinae with the minimum close to the 2009 periastron passage. The red points correspond to the high-energy events ( $E > 20$  GeV) detected by *Fermi/LAT* within  $1^\circ$  of  $\eta$  Carinae (note the event energy scale on the right).

These two results imply that the probability to find a pulsar and a blazar at the location of  $\eta$  Carinae is lower than  $10^{-9}$ .

With the above probabilities and the absence of any other bright X-ray source in the *INTEGRAL* error circle (Leyder et al. 2010), we can safely assume that the high-energy emission detected by *Fermi* and *INTEGRAL* comes from a single source, very likely  $\eta$  Carinae.

*Chandra* images of  $\eta$  Carinae (Weis et al. 2004) show an extended soft shell-like component (corresponding to an external shock at the boundary of the *Homunculus* nebula) around the harder, point-like emission. Ohm et al. (2010) have argued that the gamma-ray emission detected by *Fermi* could be emitted by this external shock. Their conclusion was based on the first eleven month spectrum, which did not exhibit the two spectral components presented above. The high-energy spectral component cannot be explained by the external shock, because the density is far too low to allow significant hadron interactions and  $\pi^0$  cooling. In addition, Leyder et al. (2010) have shown that the contribution of this outer shell to the hard X-ray emission from  $\eta$  Carinae was lower than 15%. Thus the outer shell interpretation seems unlikely.

#### 3.2. Particle acceleration in $\eta$ Carinae

We will assume below that particle acceleration takes place in  $\eta$  Carinae through diffusive shock acceleration in the colliding wind region of the binary system. In the shock region, particle acceleration is counterbalanced by four main cooling processes:

1. **Inverse Compton scattering** of electrons in the intense ultraviolet radiation field of the stars. The cooling time scale is

$$t_{IC} = \frac{3\gamma m_e c^2}{4\sigma_T c \gamma^2 \beta^2 U_{rad}} = \frac{3\pi R^2 m_e c^2}{\sigma_T \gamma \beta^2 L} \approx \frac{R_{10^{14}\text{cm}}^2}{\gamma_{10^4} L_{5 \cdot 10^6 L_\odot}} \times 6 \cdot 10^2 \text{ s},$$

where  $L$  is the stellar ultraviolet luminosity of the primary star and  $R$  is its distance to the colliding wind region.

2. **Proton-proton interactions** and subsequent pion decay. Bednarek (2005) pointed out that high-energy hadrons in the wind of massive stars will be photo-disintegrated into protons and neutrons on a short timescale. The interaction

timescale for protons is inversely proportional to the density of matter in the post-shock region, where the particles are trapped by the magnetic field. Hydrodynamic simulations (Pittard 2009) indicate that the density in the shock region is much larger than the unperturbed wind density, by a factor of  $\delta \sim 1\text{--}100$ . The p-p cooling time scale can therefore be written :

$$t_{pp} = \frac{1}{\sigma_{pp}\delta n c} = \frac{4\pi R_{sh}^2 m_p V_w}{\sigma_{pp}\delta \dot{M} c} \approx \frac{R_{10^{14}\text{cm}}^2 V_{10^3\text{km/s}}}{\delta_{10} \dot{M}_{10^{-4}M_{\odot}/\text{yr}}} \times 4 \cdot 10^5 \text{ s},$$

where  $V$  is the typical wind velocity and  $\dot{M}$  is the mass loss rate of the primary star.

- Proton diffusion** away from the shock region. The diffusion timescale is related to the bulk velocity of the post-shock material from the central regions towards the outside. Hydrodynamic simulations indicate that the material flows out of the shock region at a velocity smaller than, but of the order of, the pre-shock wind velocity (Pittard 2009). As the shock region has a size similar to the stellar separation, the bulk diffusion timescale can be estimated as (Bednarek 2005) :

$$t_{bulk} = 3R/V \approx \frac{R_{10^{14}\text{cm}}}{V_{10^3\text{km/s}}} \times 3 \cdot 10^6 \text{ s}.$$

- Electron bremsstrahlung** in the post-shock region. For a density

$$\delta n = \delta \frac{\dot{M}}{4\pi R^2 V m_p} \approx \frac{\delta_{10} \dot{M}_{10^{-4}M_{\odot}/\text{yr}}}{R_{10^{14}\text{cm}}} \times 3 \cdot 10^9 \text{ cm}^{-3},$$

the cooling timescale is given by (Aharonian 2004) :

$$t_{br} \approx 1.2 \times 10^{15} (\delta n_{\text{cm}^{-3}})^{-1} \text{ s} \approx 4 \cdot 10^5 \text{ s}.$$

Particle acceleration in the shock is therefore mainly counterbalanced by Inverse Compton scattering for electrons and by proton-proton interactions. Equating the acceleration time  $t_{acc} = \frac{R_L}{c} \left(\frac{c}{v}\right)^2$  respectively with  $t_{IC}$  and  $t_{pp}$  for electrons and protons ( $R_L$  is the Larmor radius) provides the maximum characteristic energy of the particle distribution.

For electrons, a powerlaw spectrum is expected, with an exponential cutoff at an energy

$$\gamma_{max,e} = \sqrt{\frac{3\pi e c^2}{\sigma_T \beta^2}} \sqrt{\frac{B \cdot R^2}{L}} \frac{V}{c} \approx \sqrt{\frac{B_{1G} \cdot R_{10^{14}\text{cm}}^2}{L_{5 \cdot 10^6 L_{\odot}}}} V_{10^3\text{km/s}} \times 3 \cdot 10^4,$$

where  $B$  is the magnetic field in the shock region.

$\gamma_{max,e}$  should be fairly independent of the orbital position in the dipole approximation for a magnetic field varying as  $R^{-2}$ . The gamma-ray spectrum will therefore feature an exponential cutoff at the maximal energy as derived by Eichler & Usov (1993). A cutoff energy of  $\sim 1$  GeV (Sect. 2.3) corresponds to a magnetic field of  $\sim 50$  G at the stellar surface.

For protons, the maximum characteristic energy is limited by proton-proton interactions to

$$\gamma_{max,p} = \frac{4\pi R^2 e B}{\sigma_{pp} \delta \dot{M}} \left(\frac{V}{c}\right)^3 \approx \frac{R_{10^{14}\text{cm}}^2 B_{1G} V_{10^3\text{km/s}}^3}{\delta_{10} \dot{M}_{10^{-4}M_{\odot}/\text{yr}}} \times 4 \cdot 10^4.$$

The non-thermal spectral energy distribution of  $\eta$  Carinae has been represented with a model consisting of two cutoff powerlaw distributions for the electrons and for the interacting protons. The model and the data are shown together in Fig. 5. The

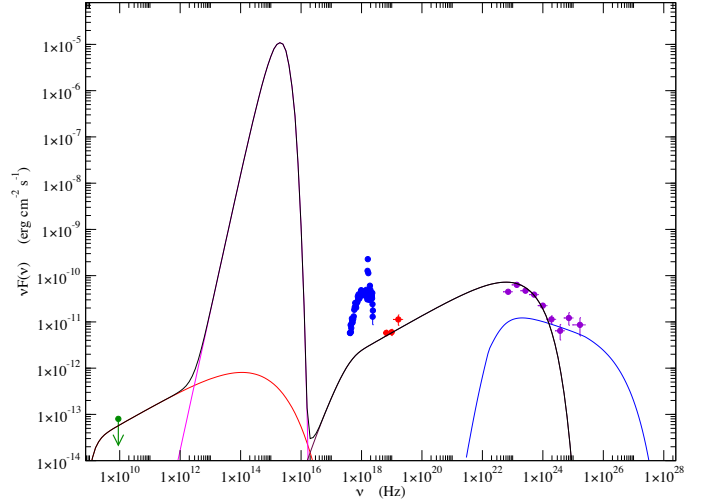


**Fig. 5.** Spectral energy distribution of  $\eta$  Carinae including *BeppoSAX/MECS* (blue), *INTEGRAL/ISGRI* (red) and *Fermi/LAT* (purple) data, and a radio upper limit to the synchrotron emission (green). From low to high energies are shown the synchrotron, stellar emission, inverse Compton and  $\pi^0$ -decay spectral components.

**Table 1.** Model parameters of the shock region determining the non-thermal spectral components of  $\eta$  Carinae, as displayed in Fig. 5.

	Parameter	Value
Environment	Photon energy density	2.7 erg/cm <sup>3</sup>
	Magnetic field	0.5 G
	Density	3 · 10 <sup>9</sup> cm <sup>-3</sup>
Electron distribution	Powerlaw index	2.25
	$\gamma_{max,e}$	10 <sup>4</sup>
	Total energy	10 <sup>40</sup> erg
Proton distribution	Powerlaw index	2.25
	$\gamma_{max,p}$	10 <sup>4</sup>
	Total energy	1.3 · 10 <sup>40</sup> erg

parameters of the model are listed in Table 1. The magnetic field and the electron energy distribution were adjusted to match the upper limit on the radio synchrotron emission, derived from the minimal thermal emission detected with *ACTA* (Duncan & White 2003), and to match the inverse Compton continuum determined by *INTEGRAL* and *Fermi*. The slope and cutoff energy of the interacting proton energy distribution were fixed to 2.25 and 10<sup>4</sup>, respectively, and its normalization was fitted to match the high-energy gamma-ray tail using the  $\pi^0$ -decay model of Kelner et al. (2006). The proton and ultraviolet photon energy densities in the shock region were fixed to the values expected for an average distance  $R = 10^{14}$  cm.

### 3.3. Energetic Considerations

The wind momentum ratio of  $\eta$  Carinae is  $\eta = (\dot{M}_2 V_2)/(\dot{M}_1 V_1) \approx 0.2$  (Pittard & Corcoran 2002). The half-opening angle of the shock region is therefore  $\sim 1$  rad, the fraction of the wind involved in the wind collision region is  $\sim 10\%$ , and the mechanical energy available in that region is  $\sim 200 L_{\odot}$ .

For a density of cold protons of  $3 \cdot 10^9 \text{ cm}^{-3}$  in the shock region, the normalization of the  $\pi^0$ -decay spectrum (Fig. 5) requires a total interacting proton energy  $E_p \sim 10^{40}$  erg. The energy injected in the shock to sustain the observed proton distribution is of the order of  $E_p/t_{pp} \sim 10 L_\odot$ .

The gamma-ray spectrum of  $\eta$  Carinae thus indicates that  $\sim 5\%$  of the shock mechanical energy (or less than 1% of the total wind mechanical luminosity) is transferred to accelerated protons downstream. This is in agreement with recent numerical simulations of relativistic collisionless shocks (Spitkovsky 2008), if a significant fraction of the hadrons interacts and generates  $\pi^0$ .

Modeling the thermal X-ray emission depends on detailed hydrodynamical simulations (see e.g. Pittard & Corcoran 2002) and could be affected by many phenomena (Parkin et al. 2009). Such simulations can explain an X-ray luminosity of  $\approx 20 L_\odot$  above a few keV. Our analysis hence indicates that the fraction of the shock energy accelerating protons is similar to that emitting observable X-rays in  $\eta$  Carinae.

The ratio between the inverse Compton or  $\pi^0$ -decay and the X-ray emission observed in  $\eta$  Carinae is larger than predicted by existing models applied to WR 140 (Pittard & Dougherty 2006; Reimer et al. 2006). The high-energy emissivity predicted for WR140 is however not well constrained and varies by a factor of 100 depending on the model parameters. The strong inverse Compton emission and the enhanced  $\pi^0$ -emission (when compared to the X-ray emission) might be related to the strong ultraviolet photon field and to the very high density in the wind collision region of  $\eta$  Carinae, strengthening simultaneously the proton-proton collision rate and the absorption of the thermal emission. Detailed modeling is outside the scope of this paper, but these observations of  $\eta$  Carinae provide the first observational constraint on the fraction of the mechanical power injected into particle acceleration.

### 3.4. On the detection of neutrinos

The high-energy gamma-rays observed in  $\eta$  Carinae are likely produced by  $\pi^0$ -decay, a process which produces as many neutrinos as gamma-rays. Thus, the detection of neutrinos would provide a conclusive evidence that hadronic acceleration is at work in  $\eta$  Carinae.

The neutrino spectrum resulting from the decay of  $\pi^0$  has been studied by Kappes et al. (2007). In the case of  $\eta$  Carinae, and based on  $\gamma_{max,p} \sim 10^4$ , the expected spectrum is

$$\frac{dN_\nu}{dE_\nu} \approx \left( \frac{E_\nu}{1 \text{ TeV}} \right)^{-2.35} e^{-\sqrt{E_\nu}/0.25 \text{ TeV}} \times 10^{-12} (\text{cm}^2 \text{ s TeV})^{-1}.$$

The atmospheric neutrino background is far too high to expect any detection at such a low energy. However, since we have not measured the high-energy cutoff of the  $\pi^0$ -decay emission, we cannot exclude that Cherenkov experiments might detect  $\eta$  Carinae at energies higher ( $\gamma_{max,p} \gtrsim 10^5$ ) than anticipated. Unfortunately, even in that case, only a few neutrinos could be detected by *KM3Net* in 5 years of observations, not enough for a source detection.

### 3.5. Other sources

The density and magnetic field in the vicinity of the shock in  $\eta$  Carinae are such that a large fraction of the energy carried by high-energy protons is converted to gamma-rays. Systems

with lower stellar winds or magnetic fields will feature fainter  $\pi^0$ -decay emission.

Scaling the emissivity of  $\eta$  Carinae by the mass loss rate (i.e. the wind density) suggests that LBV systems could be detected by *Fermi* up to the Galactic center while WR or OB systems could be detected within 1 kpc and 0.1 kpc, respectively. Very few objects could therefore be detected. OB associations could have a combined stellar mass loss rate as strong as  $\eta$  Carinae and similar efficiency in creating  $\pi^0$  (Ozernoy et al. 1997). They could thus be detected up to distances of several kpc, although their extended emission is more difficult to measure, especially in the Galactic plane.

The mechanical energy in the stellar wind of a massive star, integrated over its lifetime, could reach some  $10^{50}$  erg. From an energetic point of view, extrapolating on the particle acceleration efficiency of  $\eta$  Carinae, stellar winds ejected during the massive star evolution in a suitable environment could be as effective as a SNR to accelerate hadrons. Future Cherenkov observations will tell if stellar wind collisions could accelerate particles up to the knee of the cosmic-ray spectrum.

## 4. Conclusions

We have detected a bright gamma-ray source at the position of  $\eta$  Carinae using 21 months of *Fermi/LAT* data. Its flux at a few 100 MeV corresponds very well to the extrapolation of the hard X-ray spectrum of  $\eta$  Carinae (as measured by *INTEGRAL* and *Suzaku*) towards higher energies. The spectral energy distribution, which corresponds to an average over almost half of the orbit of  $\eta$  Carinae, features two spectral components.

The first one is a powerlaw extending from keV to GeV energies, with an exponential cutoff at  $\sim 1$  GeV. This component can be understood assuming inverse Compton scattering of stellar photons by electrons accelerated up to  $\gamma \sim 10^4$  in the wind collision region. The observed cutoff energy implies a magnetic field  $\sim 50$  G at the stellar surface.

The second component, a hard gamma-ray tail, is detected above 20 GeV. This bright component could be explained by  $\pi^0$ -decay of accelerated hadrons interacting with the dense stellar wind in the shock region. The ratio between the fluxes of the  $\pi^0$  and inverse Compton components is roughly as predicted by simulations (Pittard & Dougherty 2006; Reimer et al. 2006). Bremsstrahlung emission is expected at a much lower level and with a cutoff energy similar to that of the inverse Compton component.

The hard gamma-ray tail can only be understood if emitted close to the wind collision region. Indeed, the external shock between the *Homunculus* nebula and the interstellar medium occurs at a density and magnetic field strength that are much too small to explain the observed emission. It is possible that a part of the soft gamma-ray emission comes also from inverse Compton scattering of infrared photons in the external shock as suggested by Ohm et al. (2010) (see also Leyder et al. 2010). It is however difficult to account for the hard tail without a significant fraction of the soft gamma-ray emission being emitted by the colliding wind region. Detection of any hard X-ray or soft gamma-ray variability would rule out the external shock model.

The energy transmitted to the accelerated particles ( $\sim 5\%$  of the wind collision mechanical energy) is of the same order as that of the observed thermal X-ray emission, providing an important observational constraint for future numerical hydrodynamical models of the colliding wind region in  $\eta$  Carinae.

With the exception of the short flare detected by *Agile*, the averaged hard X-ray (Leyder et al. 2010) and soft gamma-ray



emissions do not vary by more than 50% along the orbit, not even during the periastron passage. This provides an interesting constraint on the evolution of the magnetic field and of the wind collision region along the orbit.

We finally suggest that Cherenkov telescopes could measure the hadronic cutoff energy in  $\eta$  Carinae.

## References

- Abdo, A. A., Ackermann, M., Ajello, M., et al. 2009, *ApJ. Supp.*, 183, 46  
 Abdo, A. A., Ackermann, M., Ajello, M., et al. 2010, *ApJ. Supp.*, 187, 460  
 Abraham, Z., Falceta-Gonçalves, D., Dominici, T. P., et al. 2005, *A&A*, 437, 977  
 Aharonian, F. A. 2004, *Very high energy cosmic gamma radiation : a crucial window on the extreme Universe* (River Edge, NJ: World Scientific Publishing)  
 Andriess, C. D., Donn, B. D., & Viotti, R. 1978, *MNRAS*, 185, 771  
 Atwood, W. B., Abdo, A. A., Ackermann, M., et al. 2009, *ApJ*, 697, 1071  
 Axford, W. I. 1981, *Annals of the New York Academy of Sciences*, 375, 297  
 Bednarek, W. 2005, *MNRAS*, 363, L46  
 Benaglia, P. & Romero, G. E. 2003, *A&A*, 399, 1121  
 Cash, W. 1979, *ApJ*, 228, 939  
 Casse, M. & Paul, J. A. 1982, *ApJ*, 258, 860  
 Corcoran, M. F. 2005, *AJ*, 129, 2018  
 Corcoran, M. F. & Hamaguchi, K. 2007, in *Revista Mexicana de Astronomia y Astrofisica Conference Series*, Vol. 30, 29–34  
 Damineli, A. 1996, *ApJ*, 460, L49  
 Damineli, A., Hillier, D. J., Corcoran, M. F., et al. 2008, *MNRAS*, 384, 1649  
 Damineli, A., Kaufer, A., Wolf, B., et al. 2000, *ApJ*, 528, L101  
 Davidson, K., Gull, T. R., Humphreys, R. M., et al. 1999, *AJ*, 118, 1777  
 Davidson, K. & Humphreys, R. M. 1997, *ARA&A*, 35, 1  
 De Becker, M. 2007, *A&A Rev.*, 14, 171  
 Duncan, R. A. & White, S. M. 2003, *MNRAS*, 338, 425  
 Duncan, R. A., White, S. M., Lim, J., et al. 1995, in *Revista Mexicana de Astronomia y Astrofisica Conference Series*, ed. V. Niemela, N. Morrell, & A. Feinstein, Vol. 2, 23–+  
 Eichler, D. & Usov, V. 1993, *ApJ*, 402, 271  
 Fernández-Lajús, E., Fariña, C., Calderón, J. P., et al. 2010, *New Astronomy*, 15, 108  
 Hartman, R. C., Bertsch, D. L., Bloom, S. D., et al. 1999, *VizieR Online Data Catalog*, 212, 30079  
 Hillier, D. J., Davidson, K., Ishibashi, K., & Gull, T. 2001, *ApJ*, 553, 837  
 Iping, R. C., Sonneborn, G., Gull, T. R., Massa, D. L., & Hillier, D. J. 2005, *ApJ*, 633, L37  
 Kappes, A., Hinton, J., Stegmann, C., & Aharonian, F. A. 2007, *Journal of Physics Conference Series*, 60, 243  
 Kelner, S. R., Aharonian, F. A., & Bugayov, V. V. 2006, *Phys. Rev. D*, 74, 034018  
 Leyder, J., Walter, R., & Rauw, G. 2008, *A&A*, 477, L29  
 Leyder, J., Walter, R., & Rauw, G. 2010, *A&A*, in press  
 Mattox, J. R., Bertsch, D. L., Chiang, J., et al. 1996, *ApJ*, 461, 396  
 Nielsen, K. E., Corcoran, M. F., Gull, T. R., et al. 2007, *ApJ*, 660, 669  
 Ohm, S., Hinton, J. A., & Domainko, W. 2010, *ArXiv e-prints*  
 Ozernoy, L. M., Genzel, R., & Usov, V. V. 1997, *MNRAS*, 288, 237  
 Parkin, E. R., Pittard, J. M., Corcoran, M. F., Hamaguchi, K., & Stevens, I. R. 2009, *MNRAS*, 394, 1758  
 Pittard, J. M. 2007, *ApJ*, 660, L141  
 Pittard, J. M. 2009, *MNRAS*, 396, 1743  
 Pittard, J. M. & Corcoran, M. F. 2002, *A&A*, 383, 636  
 Pittard, J. M. & Dougherty, S. M. 2006, *MNRAS*, 372, 801  
 Reimer, A., Pohl, M., & Reimer, O. 2006, *ApJ*, 644, 1118  
 Sekiguchi, A., Tsujimoto, M., Kitamoto, S., et al. 2009, *ArXiv e-prints*  
 Seward, F. D., Butt, Y. M., Karovska, M., et al. 2001, *ApJ*, 553, 832  
 Smith, N. 2006, *ApJ*, 644, 1151  
 Smith, N., Gehrz, R. D., Hinz, P. M., et al. 2003, *AJ*, 125, 1458  
 Spitkovsky, A. 2008, *ApJ*, 682, L5  
 Stevens, I. R., Blondin, J. M., & Pollock, A. M. T. 1992, *ApJ*, 386, 265  
 Tavani, M., Sabatini, S., Pian, E., et al. 2009, *ApJ*, 698, L142  
 Usov, V. V. 1992, *ApJ*, 389, 635  
 van Boekel, R., Kervella, P., Schöller, M., et al. 2003, *A&A*, 410, L37  
 Verner, E., Bruhweiler, F., & Gull, T. 2005, *ApJ*, 624, 973  
 Viotti, R. F., Antonelli, L. A., Rossi, C., & Rebecchi, S. 2004, *A&A*, 420, 527  
 Weis, K., Corcoran, M. F., Bomans, D. J., & Davidson, K. 2004, *A&A*, 415, 595  
 Whitelock, P. A., Feast, M. W., Koen, C., Roberts, G., & Carter, B. S. 1994, *MNRAS*, 270, 364  
 Whitelock, P. A., Feast, M. W., Marang, F., & Breedt, E. 2004, *MNRAS*, 352, 447  
 Wilks, S. 1938, *Ann. Math. Stat.*, 9, 60